



Synergy in Sn-Mn oxide boosting the hydrogenation catalysis of supported Pt nanoparticles for selective conversion of levulinic acid

Yaowei Lu^a, Yongxing Wang^a, Qinghu Tang^b, Qiue Cao^a, Wenhao Fang^{a,*}

^a School of Chemical Science and Technology, Key Laboratory of Medicinal Chemistry for Natural Resource - Ministry of Education, National Demonstration Center for Experimental Chemistry and Chemical Engineering Education, Yunnan University, 2 North Cuihu Road, 650091 Kunming, China

^b School of Chemistry and Chemical Engineering, Henan Normal University, 453007 Xinxiang, China

ARTICLE INFO

Keywords:

Bifunctional catalyst
Hydrogenation-dehydration
Lewis acidic sites
Lower energy barrier
Metal-support interaction
Synergistic effect

ABSTRACT

The synergistic effect in a bimetallic oxide usually plays a vital role in determining the behavior of supported-metal catalysts. We show the unique synergy in a $\text{Sn}_x\text{Mn}_y\text{O}_z$ oxide, which can boost the hydrogenation catalysis of supported Pt nanoparticles for selective conversion of levulinic acid (LA) to γ -valerolactone (GVL). On a series of $\text{Pt}/\text{Sn}_x\text{Mn}_y\text{O}_z$ catalysts with a similar Pt loading (ca. 0.44 wt%) and a controlled Pt size (ca. 2.7 nm), the intrinsic TOF presents a volcano-like dependence on Pt^0 sites and Lewis acidity, which is determined by the variable synergistic effect between MnO_y and SnO_y . The optimal $\text{Pt}/\text{Sn}_{0.8}\text{Mn}_1\text{O}_y$ catalyst exhibits a high $i\text{TOF}$ of 2709 h^{-1} and achieves 100% selectivity to GVL at 99% conversion of LA at 120°C and 2 MPa of H_2 . DFT calculations demonstrate that the incorporation of Sn can provide a lower energy barrier for the crucial elementary reactions.

1. Introduction

The sustainable conversion of renewable and abundant lignocellulosic biomass into fuels and chemicals has received a large consensus [1–3]. γ -Valerolactone (GVL) is identified as an important bio-platform molecule that allows offering a tremendous flexibility to down-stream applications. For instance, GVL can be widely used as fuel additive, food ingredient, and intermediate for fine chemical synthesis [4,5]. Besides, it can serve as a high-quality solvent for bio-refining processes [6]. The catalytic hydrogenation of levulinic acid (LA) is envisioned to be a primary route to produce GVL [7–12]. Because LA can be readily prepared from cellulose and hemicellulose through an acid hydrolysis [13]. Scheme 1 illustrates that hydrogenation of LA undergoes a two-step reaction pathway that involves tandem hydrogenation and intramolecular dehydration in the opposite sequence. Usually, the major route would yield 4-hydroxypentanoic acid (HPA) as the intermediate, which is favored in thermodynamics as shown from theoretical and experimental analyses [14]. Therefore, a performant hydrogenation catalyst integrated with Lewis acidic sites is believed to benefit an excellent selectivity to GVL at a high conversion of LA [4].

Supported-Pt nanoparticles have been well recognized as highly efficient hydrogenation catalyst for various unsaturated bonds (i.e.,

$\text{C}\equiv\text{C}$, $\text{C}=\text{C}$ and $\text{C}=\text{O}$) owing to the outstanding ability of Pt species on activating hydrogen in H_2 and organics [15–17]. Recently, Pt nanoparticles encapsulated in an acidic H-ZSM-5 zeolite showed an advantage on the complex tandem catalysis for hydrogenation-dehydration of bio-derived furfural, owing to the cooperative ability on the basis of multi-functional sites on the catalyst [18,19]. However, very few supported Pt nanoparticles have been reported to date as the selective heterogeneous catalysts for hydrogenation of LA to GVL [20–22]. Specifically, a $\text{Pt}_{40}/\text{meso-SiO}_2$ catalyst afforded 88% conversion of LA and 98% selectivity to GVL at 150°C and 1 MPa H_2 [20], while a Pt/zeolite-Y catalyst provided 92% selectivity at 100% conversion at 220°C and 2.5 MPa H_2 [21]. Another Pt/ Al_2O_3 catalyst may give a similar performance under mild conditions (i.e., 70°C and 0.13 MPa H_2) but need assistance of extra bio-reductants [22]. Clearly, either the conversion or the selectivity is far less satisfying. In fact, the turnover frequency values (TOF) of those catalysts are rather low ($13.5\text{--}27.1 \text{ h}^{-1}$). On the other hand, alloying a second metal has been shown as an effective approach to improve the intrinsic activity of Pt catalysts. For example, a $\text{Pt}_1\text{Pd}_3/\text{SBA-15}$ and a $\text{PtNb}/\text{BP2000}$ bimetallic catalyst can offer an outstanding TOF of 3600 and 2376 h^{-1} at 99% selectivity to GVL [23,24], respectively. Nonetheless, the necessary use of quite high temperature ($180\text{--}220^\circ\text{C}$) and pressurized H_2 (4–10 MPa)

* Corresponding author.

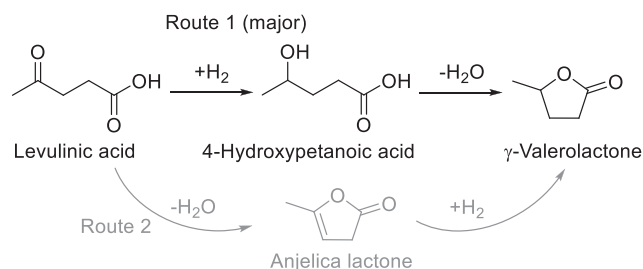
E-mail address: wenhao.fang@ynu.edu.cn (W. Fang).

<https://doi.org/10.1016/j.apcatb.2021.120746>

Received 22 June 2021; Received in revised form 18 September 2021; Accepted 20 September 2021

Available online 23 September 2021

0926-3373/© 2021 Elsevier B.V. All rights reserved.



Scheme 1. Reaction pathway and possible products for the catalytic hydrogenation of LA.

is still a big concern, which may not only consume excessive energy but also incur potential safety issue.

Apart from the active metal, the performance of Pt towards hydrogenation reactions can be greatly promoted by the synergy between different components in the support. For instance, during the reductive amination of LA to pyrrolidones, it was disclosed that an acid-base interaction between the acidic sites on MoO_x/TiO₂ and the C=O bond in LA or intermediate enabled to achieve a superior activity of the supported Pt catalyst [25]. In another case, the stress between the bulk γ-Mo₂N phase and surface MoO_x species was demonstrated to induce vast active oxygen vacancies that can sustainably enhance the ability of Pt clusters in activating CO and H₂O for the water-gas shift reaction [26]. Herein, this work aims to develop a highly efficient bifunctional Pt catalyst and boost its hydrogenation performance by making full use of the synergy in the binary oxide support. Our strategy is to incorporate Sn to a home-made manganese oxide (MnO_y) to modify the pristine property on structure, redox, and acidity of MnO_y. Manipulating the different loadings of Sn in the Sn_xMn_{1-y}O_y (0.2 ≤ x ≤ 2) binary oxide support can give a rise to a variable synergistic effect between MnO_y and SnO_y oxides, which in return allows boosting the hydrogenation catalysis of supported Pt nanoparticles for GVL production from LA. To the best of our knowledge, this strategy has been scarcely reported in the literature. In addition, some advanced techniques including HAADF-STEM, *in situ* DRIFT spectrometry and DFT calculations are used to get insight into the active sites, reaction pathway and energy barrier for the elementary steps. These findings may shed a light on developing efficient metal catalyst for selective hydrogenation of bio-derived unsaturated molecules and lead to an open discussion on the reaction mechanism.

2. Experimental

2.1. Materials and reagents

All the chemicals were obtained from commercial sources and directly used. H₂PtCl₆·6H₂O (99.9%), SnCl₂·2H₂O (98%), Mn(NO₃)₂·4H₂O (98%) and 1,4-dioxane (>99%) were obtained from Alfa Aesar. Polyvinylpyrrolidone (PVP, >98%, M.W. = 10,000) was purchased from Tokyo Chemical Industry Co. Ltd. NaBH₄ (98%) was purchased from Acros Organics. Methanol (99.5%) and triethylamine (TEA, 99%) were purchased from Aladdin. Levulinic acid (LA, 99%), 4-hydroxypentanoic acid (HPA, 99%) and γ-valerolactone (GVL, > 98%) were purchased from Adamas.

2.2. Synthesis of catalysts

Sn-Mn mixed oxides with variable Sn/Mn molar ratios (*i.e.*, 0.2, 0.5, 0.8, 1 and 2) were synthesized by co-precipitation method. Typically, 15 mmol of Mn(NO₃)₂·4H₂O and 12 mmol of SnCl₂·2H₂O were dissolved in 150 mL of methanol-deionized water solution (MeOH/H₂O = 2/1, in volume). Then, TEA was dropwise added under stirring at 600 rpm till pH value of the suspension reached 9. The dark brown slurry was aged at 65 °C under stirring and condensation reflux for 18 h.

Afterwards, the mixture was filtered and washed with excessive deionized water till pH value of the filtrate reached 7. Finally, the resultant solid was dried at 110 °C overnight and calcined at 400 °C (2 °C min⁻¹) in air flow for 4 h to obtain the catalyst support named as Sn_xMn_{1-y}O_y (x represents the Sn/Mn molar ratio). Manganese oxide (MnO_y) and tin oxide (SnO_y) were also prepared by the same procedure.

0.5 wt% Pt/Sn_xMn_{1-y}O_y catalysts with a controlled Pt particle size were prepared by adsorption method of PVP-stabilized colloidal Pt nanoparticles. Typically, to 150 mL of PVP solution, a H₂PtCl₆·6H₂O solution (PVP/Pt = 1.2, in weight) was added and stirred at 600 rpm for 15 min at room temperature. Then, the powdery Sn_xMn_{1-y}O_y support was added and a freshly made NaBH₄ solution (NaBH₄/Pt = 5, in mole) was slowly injected into the mixture. After stirring for another 2 h, the resultant solid was recovered by filtration and washed repeatedly with an excessive hot deionized water (90 °C) and cold deionized water to completely remove PVP, Na⁺ and Cl⁻ ions. Finally, the catalyst was dried at 60 °C under vacuum for 12 h.

2.3. Characterizations of catalysts

Pt loading and Sn/Mn molar ratio were determined by inductively coupled plasma mass spectrometer (ICP-MS) on an Agilent 7500a apparatus. High resolution transmission electron microscopy (HR-TEM) was carried out on a Philips-FEITECNAI F30 field emission electron microscope with an acceleration voltage of 300 kV. The mean size of Pt nanoparticles was estimated by measuring sixty Pt particles from a series of high resolution TEM images. HAADF-STEM was performed on an atomic resolution analytical microscope (JEM-ARM 300F) operating at 300 kV. The EDS measurements were also performed on JEM-ARM 300F operating at 80 kV. CO chemisorption was performed at 30 °C on a Micromeritics Autochem II Chemisorption Analyzer and a stoichiometry of CO/Pt = 1 was used for calculating Pt dispersion. The Pt dispersion (*D_{Pt}*) was also estimated from the mean particle size from TEM using the empirical equation (*D* = 1.13/*d*):

$$D(\text{Pt}, \%) = \frac{6 \times V}{a \times d} \quad (1)$$

where *V* is the volume of Pt atom, *a* is the surface area of Pt atom and *d* is the mean particle size of Pt nanoparticles estimated by TEM (see the [supplementary material](#)). Powder X-ray diffraction (XRD) was carried out using a Rigaku TTR III Diffractometer provided with Cu Kα radiation (*k* = 1.5418 Å) and a beam voltage of 40 kV. The patterns were recorded in the 2θ domain (10–90°) with a measured step of 0.02° and a time integration of 0.2 s. The specific surface area of Sn_xMn_{1-y}O_y support was calculated by BET method from N₂ adsorption-desorption isotherm recorded at 77 K on a Micromeritics TriStar II 3020 Surface-Area Analyzer. X-ray photoelectron spectroscopy (XPS) was conducted under ultra-high vacuum on a Thermo Scientific Escalab 250Xi system with Al Kα radiation. The binding energy shift due to the surface charging was adjusted using a reference to the C 1 s line at 284.5 eV. Temperature-programmed reduction of H₂ (H₂-TPR) was conducted on a Micromeritics Autochem II Chemisorption Analyzer. 50 mg of sample was treated in a 5% H₂/Ar (in volume) mixed gas with a flow rate of 30 mL min⁻¹. The temperature was increased to 800 °C at a rate of 10 °C min⁻¹. Temperature-programmed desorption of ammonia (NH₃-TPD) was performed on a Micromeritics Autochem II Chemisorption Analyzer. 50 mg of sample loaded in a quartz reactor was pre-treated with He at 200 °C for 1 h. After cooling to 50 °C, adsorption of the probe gas was carried out by switching He to a 5% NH₃-He (in volume) mixed gas for 1 h. The gas-phase NH₃ was purged by He at the same temperature. TPD was then conducted in He flow by raising the temperature to 800 °C using a rate of 10 °C min⁻¹. The desorbed probe gas was detected on a ThermoStar GSD 301 T2 mass spectrometer. Diffuse reflectance Fourier transform infrared (DRIFT-IR) spectrometry was performed on a Thermo Scientific Nicolet iS50 FT-IR spectrometer with

Table 1Catalytic properties of the Pt/MnO_y, Pt/SnO_y and Pt/Sn_xMn_{1-y}O_y catalysts and their support materials.

catalyst	Pt (wt%) ^a	d, Pt (nm) ^b	Pt dispersion (%)		Pt ⁰ (%) ^c	Sn/Mn ratio		S _{BET} (m ² g ⁻¹) ^d
			TEM	CO adsorption		ICP	XPS	
Pt/MnO _y	0.42	2.7 ± 0.3	42	45	73.6	<i>n.d.</i>	<i>n.d.</i>	16
Pt/Sn _{0.2} Mn ₁ O _y	0.44	2.9 ± 0.2	39	41	81.0	0.28	0.26	63
Pt/Sn _{0.5} Mn ₁ O _y	0.43	2.6 ± 0.3	44	47	83.3	0.53	0.50	67
Pt/Sn _{0.8} Mn ₁ O _y	0.45	2.8 ± 0.2	40	40	88.4	0.82	0.83	74
Pt/Sn ₁ Mn ₁ O _y	0.44	2.6 ± 0.3	44	45	86.6	1.07	1.08	59
Pt/Sn ₂ Mn ₁ O _y	0.44	2.8 ± 0.3	40	42	84.7	2.09	2.13	53
Pt/SnO _y	0.46	2.6 ± 0.4	44	46	63.0	<i>n.d.</i>	<i>n.d.</i>	51

^a Measured by ICP-MS.^b Estimated from TEM.^c Fraction of surface Pt⁰ analyzed by XPS.^d Measured on the bare support.

a MCT detector with a resolution of 2 cm⁻¹ and a scanning number of 64. The sample in the form of pellet was degassed under vacuum (10⁻³ Pa) for 3 h at 300 °C in the 10-cm Demountable Gas Cell. Subsequently, it was cooled to 30 °C and the initial background spectrum was recorded. (i) For the time-resolved DRIFT-IR spectra of CO adsorption, a pure CO (99.99%) flow of 10 mL min⁻¹ was introduced to the cell for 1 h. Afterwards a He flow of 10 mL min⁻¹ was switched to thoroughly purge the free and the physisorbed CO molecules. Finally the spectrum was recorded. (ii) For the *in situ* catalytic reaction, LA was introduced into the cell by He flow at 30 °C and adsorbed for 1 h, and subsequently purged with He for 30 min to remove the physisorbed and residual LA. Afterwards, a H₂ flow (10 mL min⁻¹) was switched to the cell and the cell was heated to 120 °C (10 °C min⁻¹). The spectra of 1100–4000 cm⁻¹ with the time on stream (*i.e.*, 0, 5, 10, 30, 60, 90, 120 and 150 min) were collected. Finally, the cell was cooled to 30 °C. The reference spectra of HPA and GVL were collected at 120 °C. HPA or GVL was introduced into the cell by He flow at 30 °C and adsorbed for 1 h, and then purged with He flow for 30 min to remove the physisorbed and residual HPA or GVL. Then the cell was heated to 120 °C. (iii) For the pyridine adsorption IR spectra, the pyridine vapor was introduced to the cell for 0.5 h. Afterwards, a He flow (10 mL min⁻¹) was switched to remove the excessive pyridine for 0.5 h, then the cell was heated to 150 °C (10 °C min⁻¹) and kept for 0.5 h. Finally, the cell was cooled to 30 °C and the spectrum of 1400–1700 cm⁻¹ was recorded.

2.4. Catalytic reaction

Hydrogenation of LA was conducted in a 50 mL batch-type Teflon-lined stainless-steel autoclave with a 40 mL Teflon container. Typically, the container was loaded with 50 mg catalyst, 5 mmol LA and 10 mL 1,4-dioxane. After removal and purge of the residual air with Ar flow, 2 MPa of H₂ was pumped into the reactor till the pressure was stabilized. Afterwards, the reactor was placed in an oil bath preheated (110–130 °C) and under magnetic stirring at 900 rpm. The autoclave was quickly put into an ice water when the reaction finished. Then the used catalyst was separated by high-speed centrifugation (10,000 rpm for 10 min) and washed by ethanol and water several times to completely remove the adsorbed organic compounds. After a thorough wash and filtration the regenerated catalyst was dried at 60 °C under vacuum for 12 h for the next use.

The reaction mixture was diluted and analyzed on a Thermo Scientific TRACE 1310 gas chromatograph (GC) equipped with a flame ionization detector (FID) and a TR-5 capillary column (30 m length, 0.32 mm inner diameter, 0.25 μm film thickness). For the aqueous-phase reaction the analysis was performed on an Agilent 1260 Infinity HPLC and the details can be found from a previous report [27]. The quantification was conducted by the external standard method. LA, HPA and GVL were calibrated on the basis of the standard solutions at different concentrations. The obtained R² factors were all higher than 0.999. The conversion of LA and selectivity of products were calculated

by the following equations on the basis of the carbon balance, respectively. Carbon balance was monitored for each reaction and the values were of 99–100%, which indicated that the reported catalytic results can be reliable, thus the data was not reported. The intrinsic turnover frequency (iTOF, h⁻¹) for Pt/Sn_xMn_{1-y}O_y catalysts was defined as the moles of LA converted at the initial stage per mole of surface Pt atoms per unit time, and calculated based on the initial conversion of rate of LA and the Pt dispersion. Each reaction was at least repeated twice to guarantee a reproducible result, and the error of the data must be no more than 2%.

$$\text{Conv.}(\%) = \frac{n_{\text{LA,initial}} - n_{\text{LA,final}}}{n_{\text{LA,initial}}} \quad (2)$$

$$\text{Select.}(\%) = \frac{n_{\text{prod.}}}{n_{\text{LA,initial}} - n_{\text{LA,final}}} \quad (3)$$

$$\text{CB}(\%) = \frac{n_{\text{LA,final}} + n_{\text{prod.}}}{n_{\text{LA,initial}}} \quad (4)$$

$$\text{iTOF}(\text{h}^{-1}) = \frac{\text{initial conversion rate} \times M_{\text{Pt}}}{\text{Pt dispersion}} \quad (5)$$

2.5. DFT calculations

Density functional theory (DFT) calculations were performed in Vienna *ab initio* simulation package (VASP) with the generalized gradient approximation (GGA) using the Perdew-Burke-Ernzerhof (PBE) functional. The projected augmented wave (PAW) potentials were used to describe the ionic cores and valence electrons were also considered using a plane wave basis set with a kinetic energy cutoff of 400 eV (details in the [supplementary material](#)). Geometry optimizations were performed with the force convergency smaller than 0.05 eV Å⁻¹, where the same convergency were applied for the locating of transition states by the constrained optimizations. The original bulk structure is optimized before the construction of surfaces with the Monkhorst-Pack k-point of 4 × 4 × 4. The Mn₃O₄ (211) surfaces with 24 Mn and 32 O atoms were applied with half of the surface at the bottom fixed in all the calculations. Pt nanoparticle with 9 Pt atoms were used to describe the inter-surface between Pt and Mn₃O₄. On the other hand, 3 Mn atoms were replaced by Sn atoms at the first layer of Mn₃O₄ to investigate the effect of Sn doping. A Monkhorst-Pack k-point of 2 × 2 × 1 was applied for all the calculations on surfaces. In addition, the effect from the Hubbard U corrections were considered beyond the accuracy of DFT calculations of GGA, where U values (employed as U-J) of 4.0 and 3.5 were applied for Mn and Sn, respectively. Standard free energy corrections were performed by the equation:

$$\Delta G = \Delta E_{\text{DFT}} + \Delta E_{\text{ZPE}} + \Delta E_{\text{U}} - T\Delta S \quad (6)$$

where ΔE_{DFT} is the DFT electronic energy difference of each step, ΔE_{ZPE}, ΔE_U and ΔS are the correction of zero-point energy, inner energy and

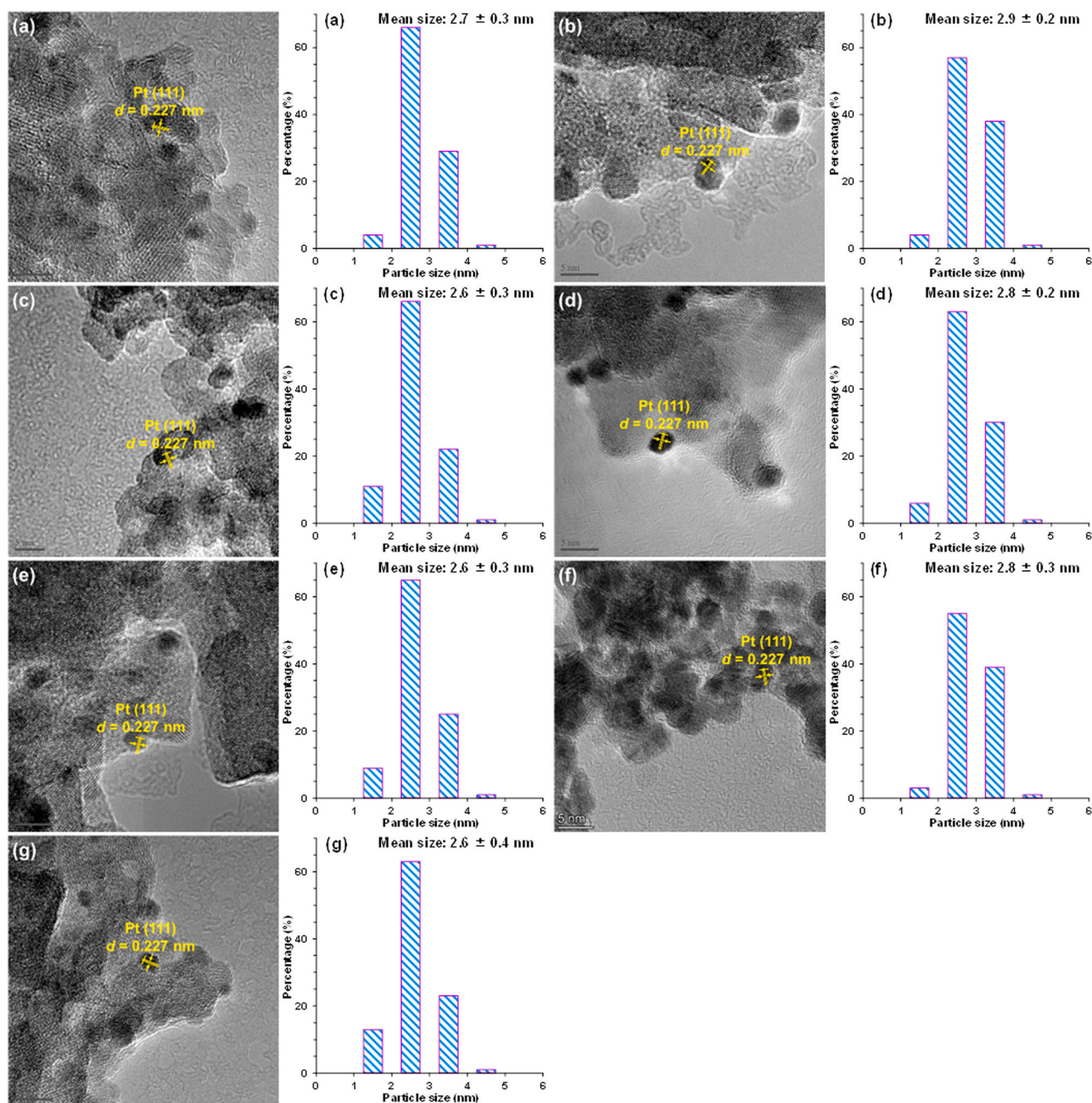


Fig. 1. HR-TEM graphs and the corresponding size distributions and mean sizes of Pt particles for the (a) Pt/MnO_y, (b) Pt/Sn_{0.2}Mn₁O_y, (c) Pt/Sn_{0.5}Mn₁O_y, (d) Pt/Sn_{0.8}Mn₁O_y, (e) Pt/Sn₁Mn₁O_y, (f) Pt/Sn₂Mn₁O_y, and (g) Pt/SnO_y catalysts.

Table 2

Catalytic performances of the Pt/MnO_y, Pt/SnO_y and Pt/Sn_xMn₁O_y catalysts for hydrogenation of LA.

Catalyst	Conv. (%) ^a	Select. (%) ^a		Conv. (%) ^b	Select. (%) ^b		<i>r</i> _{initial} (μmol g _{Pt} ⁻¹ s ⁻¹) ^b	t _{TOF} (h ⁻¹) ^b	CB ^c (%)
		GVL	HPA		GVL	HPA			
Pt/MnO _y	1	>99	<1	0.3	99	1	20	31	>99
Pt/Sn _{0.2} Mn ₁ O _y	56	96	4	11	93	7	694	1190	>99
Pt/Sn _{0.5} Mn ₁ O _y	74	98	2	15	93	7	969	1448	>99
Pt/Sn _{0.8} Mn ₁ O _y	99	100	0	25	95	5	1543	2709	100
Pt/Sn ₁ Mn ₁ O _y	68	98	2	13	94	6	821	1281	100
Pt/Sn ₂ Mn ₁ O _y	46	98	2	9	93	7	568	950	>99
Pt/SnO _y	<1	>99	<1	0.2	99	1	12	18	>99

Reaction conditions: catalyst, 50 mg; LA, 5 mmol; dioxane, 10 mL; H₂, 2 MPa; temperature, 120 °C;

^a time, 6 h;

^b time, 1 h.

^c Carbon balance.

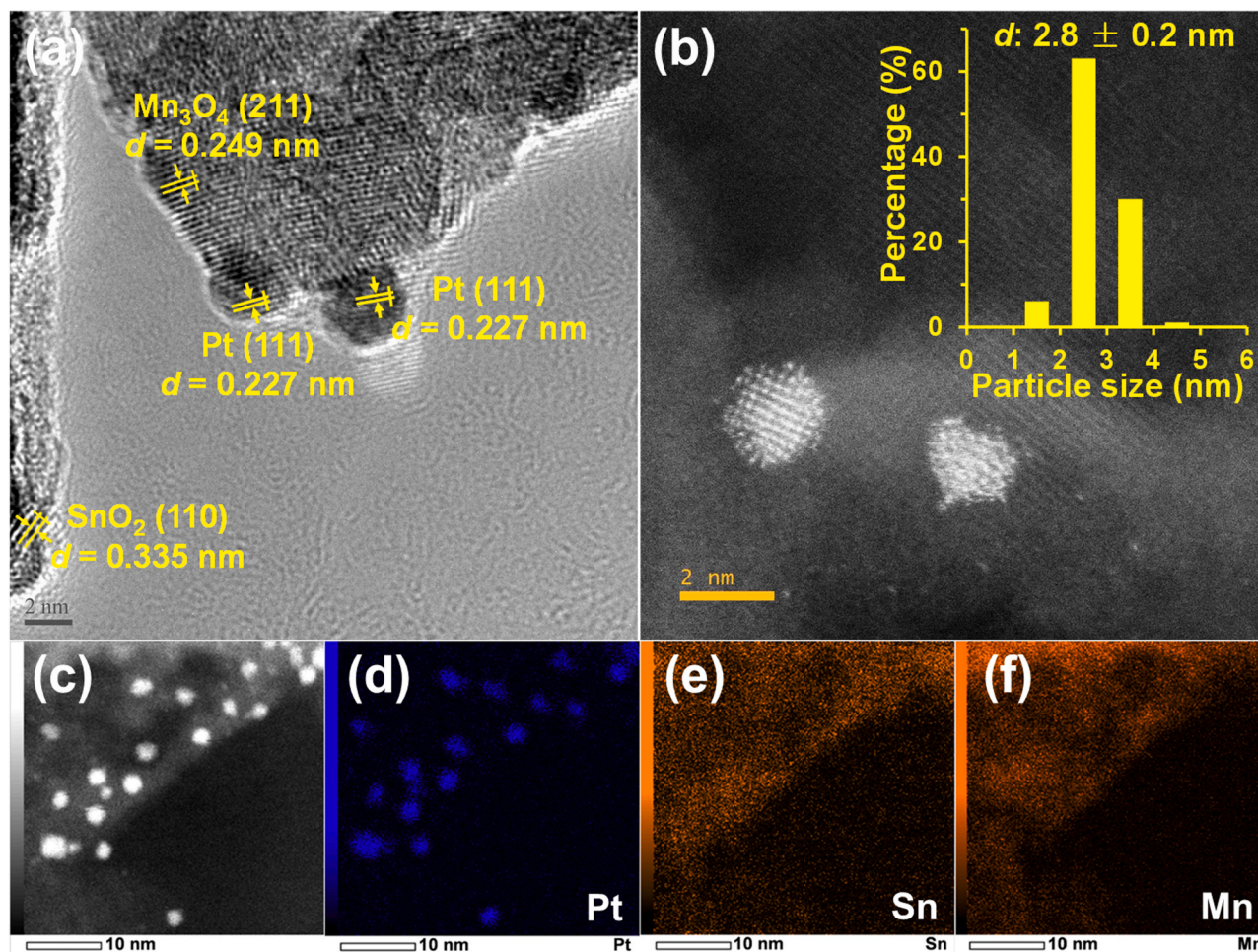


Fig. 2. (a) Bright-field STEM graph with marks of the lattice fringe for Pt nanoparticles of the $\text{Pt}/\text{Sn}_{0.8}\text{Mn}_1\text{O}_y$ catalyst. (b) HAADF-STEM graph with insertion of the corresponding size distribution of Pt nanoparticles and (c-f) color-coded EDS elemental maps for Pt, Sn and Mn of the $\text{Pt}/\text{Sn}_{0.8}\text{Mn}_1\text{O}_y$ catalyst.

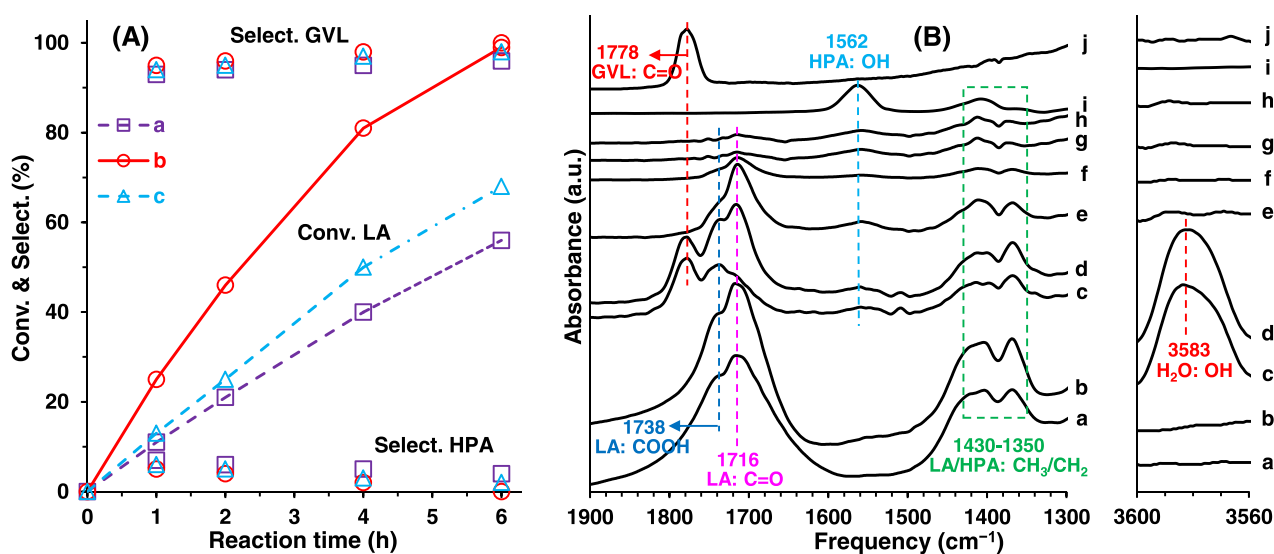


Fig. 3. (A) Time course for hydrogenation of LA over the typical $\text{Pt}/\text{Sn}_x\text{Mn}_1\text{O}_y$ catalysts. Reaction conditions: catalyst, 50 mg; LA, 5 mmol; dioxane, 10 mL; H_2 , 2 MPa; temperature, 120 °C. (a) $\text{Pt}/\text{Sn}_{0.2}\text{Mn}_{1.0}\text{O}_y$, (b) $\text{Pt}/\text{Sn}_{0.8}\text{Mn}_{1.0}\text{O}_y$, and (c) $\text{Pt}/\text{Sn}_{1.0}\text{Mn}_{1.0}\text{O}_y$. (B) Time-resolved DRIFT-IR spectra obtained during the *in situ* hydrogenation of LA in a H_2 flow (10 mL min^{-1}) at 120 °C over the $\text{Pt}/\text{Sn}_{0.8}\text{Mn}_1\text{O}_y$ catalyst. (a) 0, (b) 5, (c) 10, (d) 30, (e) 60, (f) 90, (g) 120, and (h) 150 min. The reference spectrum of chemisorbed (i) HPA and (j) GVL at 120 °C.

entropy, respectively. The free energy corrections for gas phase molecules were performed by Gaussian calculations, and the free energy corrections for adsorbates were obtained by the vibrational frequency calculations by VASP. All the energies were corrected to the temperature of 120 °C.

3. Results and discussion

3.1. The role of Pt nanoparticles

ICP-MS analysis shows that the actual loadings of the immobilized Pt on different oxides are quite similar (0.42–0.46%, in weight) but slightly lower than the theoretical value of 0.5% (Table 1). The morphology of supported catalyst is inspected by HR-TEM. As displayed in Fig. 1, either the unary or the binary oxide support presents an amorphous morphology, whereas Pt nanoparticles are found to be highly dispersed with an observation of the characteristic lattice fringe identical to the (111) facet of Pt. Moreover, the Pt sizes are confined to nearly 1–4 nm and the mean sizes are estimated to be ca. 2.7 nm regardless of the oxide supports (Fig. 1, Table 1). As expected, the Pt dispersions calculated by the empirical relationship from the mean particle size are similar. Moreover, CO chemisorption data clarify that the measured Pt dispersion is well consistent with its particle size, being ca. 40–45% (Table 1). These results demonstrate that a series of supported Pt nanoparticles with an approximate loading and a controlled diameter are effectively loaded onto the MnO_x , SnO_x and $\text{Sn}_x\text{Mn}_1\text{O}_y$ oxides.

As reported in Table 2, Pt/ MnO_x and Pt/ SnO_x as the reference catalysts are barely active for hydrogenation of LA. However, the $\text{Sn}_x\text{Mn}_1\text{O}_y$ binary oxides supported Pt shows an apparent conversion of LA (46–99%) and an excellent selectivity to GVL (96–100%). The conversion first rises and then declines by increasing the Sn content, while the selectivity also presents a similar trend. The optimal performance is obtained over the Pt/ $\text{Sn}_{0.8}\text{Mn}_1\text{O}_y$ catalyst, that is, 100% selectivity to GVL at 99% conversion of LA at 120 °C and 2 MPa of H_2 after 6 h. Notably, the bare supports are confirmed to be catalytically inactive, and moreover, the unreduced Pt/ $\text{Sn}_{0.8}\text{Mn}_1\text{O}_y$ catalyst can only afford rather a low conversion at 7% (Table S1). Further inspection on the optimal catalyst by bright-field STEM and HAADF-STEM shows that uniform and small Pt nanoparticles (ca. 2.8 nm) are highly dispersed and the (111) facet is exposed (Fig. 2). EDS elemental maps present a uniform overlap of Sn and Mn signals, and the dominant facets of Mn_3O_4 (i.e., the (211) plane) and SnO_2 (i.e., the (110) plane) are clearly observed. This body of results demonstrates that well-dispersed Pt nanoparticles in a metallic state can be the active sites for hydrogenation of LA to GVL and the synergy in the $\text{Sn}_x\text{Mn}_1\text{O}_y$ mixed oxides can obviously affect the catalytic performances of supported Pt nanoparticles.

3.2. Investigation on the reaction pathway

To investigate the reaction pathway for hydrogenation of LA over the Pt/ $\text{Sn}_x\text{Mn}_1\text{O}_y$ catalyst, the time course experiments are conducted on some typical catalysts (Fig. 3A). Conversion of LA globally increases during 6 h of reaction, meanwhile HPA as the only intermediate is slowly transformed to GVL. In addition, an appropriate Sn/Mn ratio is shown to simultaneously promote conversions of LA and HPA. To directly monitor the reaction pathway, an *in situ* hydrogenation of LA is performed in a H_2 flow at 120 °C on a DRIFT-IR spectrometer (Fig. 3B). The chemisorption of LA on the Pt/ $\text{Sn}_{0.8}\text{Mn}_1\text{O}_y$ catalyst is detected by a group of characteristic bands. The broad band centered at ca. 1716 and 1738 cm^{-1} can be attributed to the stretching vibrations of the C=O and COOH groups, while the bands in the range of 1350–1430 cm^{-1} can be related to the C–H backbone of LA [28]. When the reaction proceeds for 10–30 min, several new bands are clearly observed. The band at ca. 1778 cm^{-1} is identical to the stretching vibration of the C=O group in GVL [29], while a band at ca. 3583 cm^{-1} corresponds to the stretching vibration of the OH group in H_2O [30]. Notably, the characteristic bands

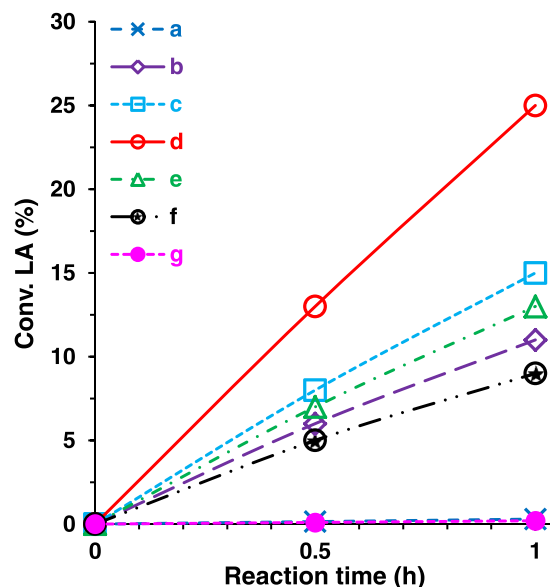


Fig. 4. Conversion of LA during the initial stage of hydrogenation over the Pt/ $\text{Sn}_x\text{Mn}_1\text{O}_y$ catalysts. Reaction conditions: catalyst, 50 mg; LA, 5 mmol; dioxane, 10 mL; H_2 , 2.0 MPa; temperature, 120 °C. (a) Pt/ MnO_y , (b) Pt/ $\text{Sn}_{0.2}\text{Mn}_1\text{O}_y$, (c) Pt/ $\text{Sn}_{0.5}\text{Mn}_1\text{O}_y$, (d) Pt/ $\text{Sn}_{0.8}\text{Mn}_1\text{O}_y$, (e) Pt/ $\text{Sn}_1\text{Mn}_1\text{O}_y$, (f) Pt/ $\text{Sn}_2\text{Mn}_1\text{O}_y$, and (g) Pt/ SnO_y .

originated from the OH group (ca. 1562 cm^{-1}) and the C–H backbone (ca. 1350–1430 cm^{-1}) of HPA are also recorded in the meantime. In addition, the bands due to the C=O and COOH groups in LA simultaneously become weaker. The above spectroscopic evidence reveals that GVL and H_2O are co-generated via HPA as the intermediate from hydrogenation and dehydration of LA. This process shows a fast response on the Pt/ $\text{Sn}_{0.8}\text{Mn}_1\text{O}_y$ catalyst. With the flowing of H_2 , GVL is prone to be desorbed from the surface of catalyst after 60 min, whereas the chemisorption of LA is more stable. This feature may be beneficial to the catalytic reaction.

3.3. The intrinsic activity of the Pt/ $\text{Sn}_x\text{Mn}_1\text{O}_y$ catalysts

To measure the intrinsic activity of the series Pt catalysts, hydrogenation of LA is investigated during the initial stage up to 1 h. As shown in Fig. 4, conversion of LA almost linearly increases upon reaction time and the values are restricted in the kinetic-controlled region. Thereby, the intrinsic turnover frequency (TOF) can be calculated from the initial conversion rate (r_{initial}) on the basis of surface exposed Pt atoms. As listed in Table 2, TOF as well as selectivity of GVL, is disclosed to apparently depend on the Sn/Mn ratio, which shows a trend from rise to decline and reaches the highest value of 2709 h^{-1} over the Pt/ $\text{Sn}_{0.8}\text{Mn}_1\text{O}_y$ catalyst. The kinetic profiles obtained at various temperatures over some typical catalysts can be linearly plotted against the reaction time (Fig. 5a–c), which is the characteristic of a first-order reaction. Previously hydrogenation of LA to GVL over supported Ru catalysts (i.e., Ru/RGO and Ru/(AlO)(ZrO)_n) was reported to be a pseudo first-order reaction [8,27]. Thereby, the apparent activation energy (E_a) can be calculated from the numerical regression by assuming a valid Arrhenius law. The kinetic data and the computational details are summarized in Table S2. It can be clearly seen from Fig. 5d that Pt/ $\text{Sn}_{0.8}\text{Mn}_1\text{O}_y$ is the most active catalyst ($E_a = 49.2 \text{ kJ mol}^{-1}$), much more active than the Pt/ $\text{Sn}_{0.2}\text{Mn}_1\text{O}_y$ ($E_a = 56.5 \text{ kJ mol}^{-1}$) and Pt/ $\text{Sn}_1\text{Mn}_1\text{O}_y$ ($E_a = 53.4 \text{ kJ mol}^{-1}$) catalysts. The kinetic results are well consistent with the synergistic effect in the $\text{Sn}_x\text{Mn}_1\text{O}_y$ supports on the catalytic performances (Table 2).

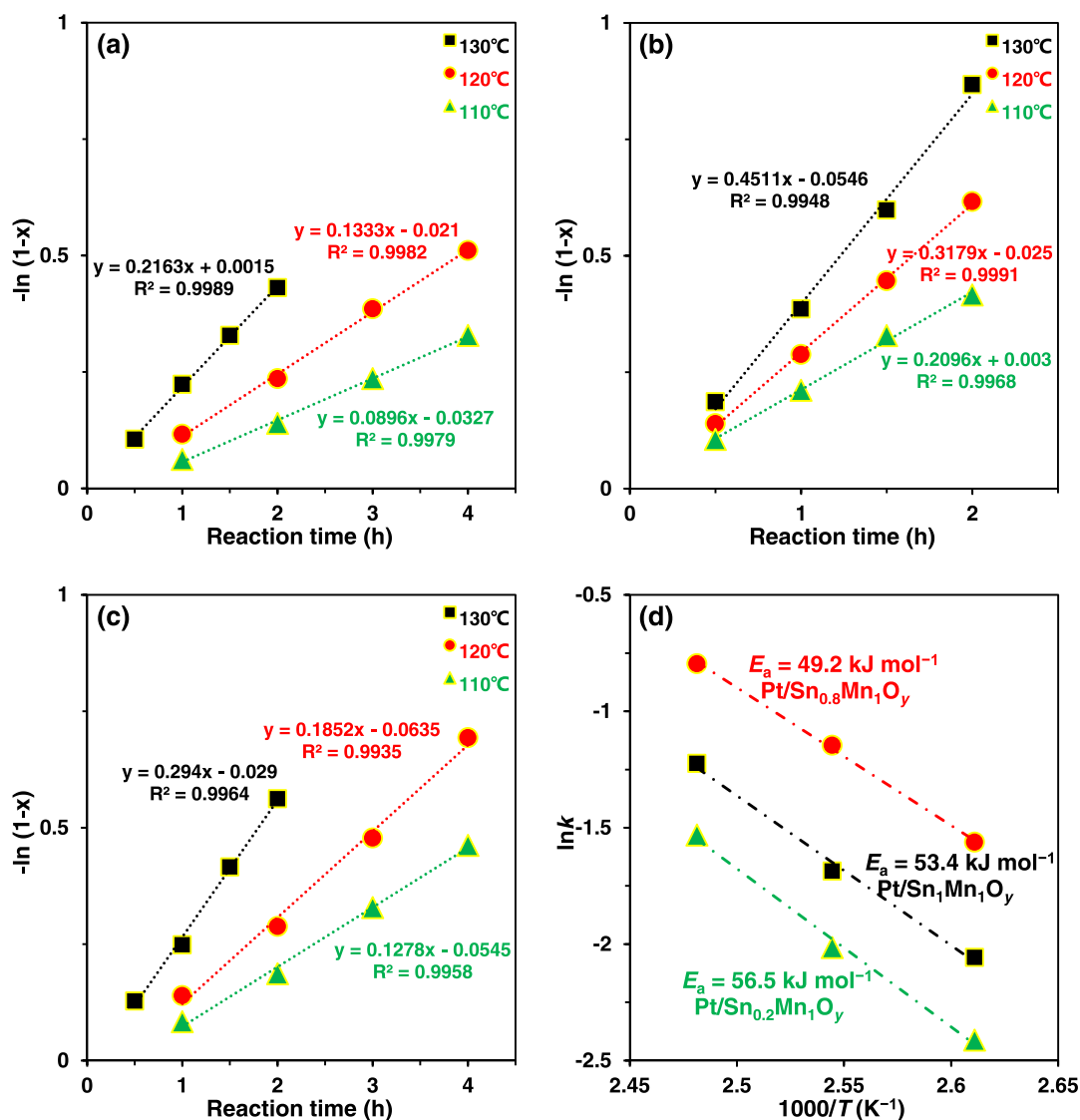


Fig. 5. Kinetic profiles for hydrogenation of LA to GVL over the typical Pt/Sn_xMn₁O_y catalysts. Reaction conditions: catalyst, 50 mg; LA, 5 mmol; dioxane, 10 mL; H₂, 2.0 MPa. (a) Pt/Sn_{0.2}Mn₁O_y, (b) Pt/Sn_{0.8}Mn₁O_y, and (c) Pt/Sn₁Mn₁O_y. (d) Arrhenius plot for hydrogenation of LA to GVL over the typical Pt/Sn_xMn₁O_y catalysts. Reaction conditions: catalyst, 50 mg; LA, 5 mmol; dioxane, 10 mL; H₂, 2 MPa; temperature, 110–130 °C.

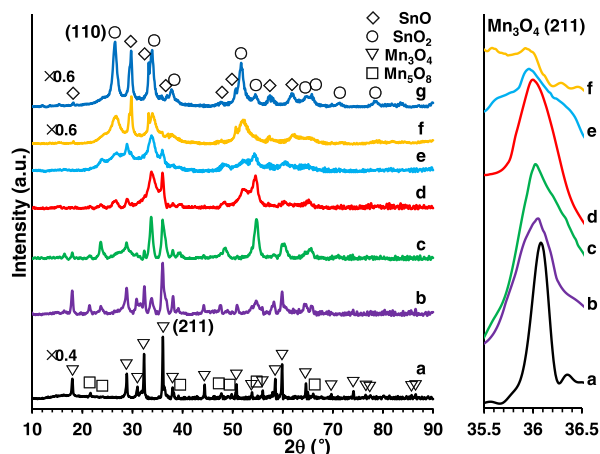


Fig. 6. XRD patterns of the (a) MnO_y, (b) Sn_{0.2}Mn₁O_y, (c) Sn_{0.5}Mn₁O_y, (d) Sn_{0.8}Mn₁O_y, (e) Sn₁Mn₁O_y, (f) Sn₂Mn₁O_y, and (g) SnO_y supports.

3.4. The synergistic effect in Sn_xMn₁O_y and the Pt-Sn_xMn₁O_y interaction

To understand such an interesting synergistic effect, the composition, structure and surface acidity of the Sn_xMn₁O_y supports are carefully analyzed. The actual Sn/Mn molar ratios determined by both ICP-MS and XPS techniques are very close to the theoretical values (Table 1), which shows the successful preparation of a series of binary oxides with a uniform distribution of Sn and Mn in the solids. As shown by XRD spectra in Fig. 6, MnO_y is composed of a tetragonal Mn₃O₄ (JCPDS #24-0734) and a monoclinic Mn₂O₃ (JCPDS #39-1218) [31,32], while SnO_y is composed of a tetragonal SnO (JCPDS #06-0395) and a tetragonal SnO₂ (JCPDS #41-1445) [33]. Particularly, Mn₃O₄ and SnO₂ are found to be the dominant phases. For the Sn_xMn₁O_y oxides, a mixed phase of MnO_y and SnO_y is observed and the diffraction peaks of MnO_y become weak as those of SnO_y grow intense by adding Sn. Moreover, the major peak due to the (211) facet of Mn₃O₄ shifts to a lower 2θ value, which can be attributed to a partial replacement of Mn ions by Sn ions (atomic radius: Sn, 1.58 Å > Mn, 1.37 Å), resulting in an expansion of the lattice distance of Mn₃O₄. As listed in Table S3, incorporating Sn ions can give rise to reducing the mean crystal size of Mn₃O₄ in the Sn_xMn₁O_y oxides compared to MnO_y. This may be related to the generation of

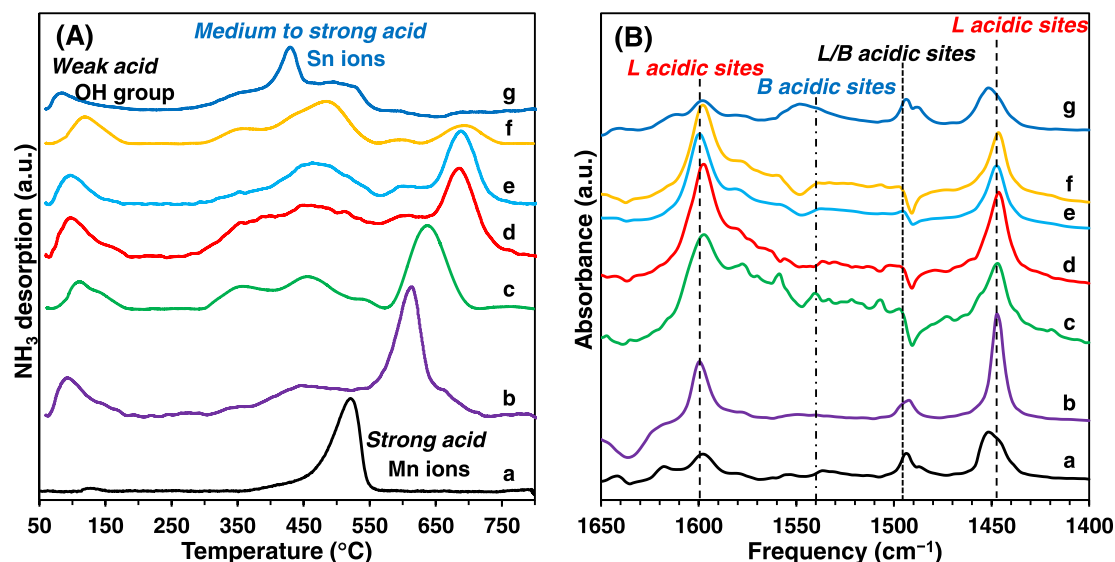


Fig. 7. (A) NH_3 -TPD profiles and (B) adsorbed pyridine-IR spectra of the (a) MnO_y , (b) $\text{Sn}_{0.2}\text{Mn}_1\text{O}_y$, (c) $\text{Sn}_{0.5}\text{Mn}_1\text{O}_y$, (d) $\text{Sn}_{0.8}\text{Mn}_1\text{O}_y$, (e) $\text{Sn}_1\text{Mn}_1\text{O}_y$, (f) $\text{Sn}_2\text{Mn}_1\text{O}_y$, and (g) SnO_y supports.

Table 3

Acidic property from the adsorbed pyridine-IR for SnO_y , MnO_y and $\text{Sn}_x\text{Mn}_1\text{O}_y$ supports.

Support	Acidity ($\mu\text{mol g}^{-1}$)			L/total
	Brønsted acidity	Lewis acidity	Total acidity	
SnO_y	114	131	245	0.53
$\text{Sn}_2\text{Mn}_1\text{O}_y$	11	253	264	0.96
$\text{Sn}_1\text{Mn}_1\text{O}_y$	20	332	352	0.95
$\text{Sn}_{0.8}\text{Mn}_1\text{O}_y$	6	411	417	0.99
$\text{Sn}_{0.5}\text{Mn}_1\text{O}_y$	28	348	376	0.93
$\text{Sn}_{0.2}\text{Mn}_1\text{O}_y$	26	328	354	0.93
MnO_y	37	247	284	0.87

higher crystal defects in the binary oxide. The specific surface areas of the $\text{Sn}_x\text{Mn}_1\text{O}_y$ supports are measured to be $53\text{--}74\text{ m}^2\text{ g}^{-1}$ (Table 1), higher than those of SnO_y ($51\text{ m}^2\text{ g}^{-1}$) and MnO_y ($16\text{ m}^2\text{ g}^{-1}$), which can be interpreted by the lattice distortions caused by a metal incorporation to the binary oxides [34,35]. Particularly, $\text{Sn}_{0.8}\text{Mn}_1\text{O}_y$ displays the highest specific surface area.

NH_3 -TPD profiles of the supports can be generally divided into two regions (Fig. 7 A). The single desorption peak at $\leq 200\text{ }^\circ\text{C}$ corresponds to the weak acidic site originated from the OH groups on an oxide surface [36], while a group of desorption peaks at $300\text{--}800\text{ }^\circ\text{C}$ are associated with the medium to strong acidic sites due to different Sn and Mn ions. MnO_y displays a peak at ca. $520\text{ }^\circ\text{C}$ that can be ascribed to the strong acidic sites due to Mn ions with different oxidation numbers [37, 38]. However, SnO_y shows three desorption peaks at ca. 350 , 430 and $510\text{ }^\circ\text{C}$, respectively. The first two peaks can be attributed to the medium to strong acidic sites associated with coordinatively unsaturated Sn^{4+} ions bearing coordination number of four and five [39], respectively. The last peak can be assigned to the strong acidic site related to four-coordinated Sn^{2+} ions [40]. More importantly, incorporating Sn can significantly modify the distribution and amount of acidic sites (Fig. 7A, Table S4). Specifically, the strong acidic sites due to Mn ions shift to higher temperatures and the acidity continuously declines. Though the medium to strong acidic sites due to Sn ions can be roughly distributed in a similar region of temperature, the acidity demonstrates a trend from rise to decline and reaches the highest value on $\text{Sn}_{0.8}\text{Mn}_1\text{O}_y$. As a result, the acidity originated from metal ions of the support is disclosed to follow the same trend and the optimal amount is also obtained on $\text{Sn}_{0.8}\text{Mn}_1\text{O}_y$.

To rationally identify Brønsted and Lewis acidic sites on the $\text{Sn}_x\text{Mn}_1\text{O}_y$ supports, the *in situ* adsorbed pyridine-IR spectroscopy is conducted. As displayed in Fig. 7B, two strong bands at 1446 and 1600 cm^{-1} can be ascribed to the Lewis acidic sites due to the adsorption of pyridine on the unsaturated Mn and/or Sn ions with different oxidation numbers [38,41]. Meanwhile, a weak band at 1540 cm^{-1} can be attributed to the characteristic Brønsted acidic sites originated from the pyridine adsorbed at OH groups on an oxide surface [41]. Another band at 1495 cm^{-1} should be assigned to the co-adsorption of pyridine on Lewis and Brønsted acidic sites [41]. Evidently, Lewis acidic sites are overwhelmed for the total acidity of the $\text{Sn}_x\text{Mn}_1\text{O}_y$ supports since the fraction of Lewis acidity to total acidity is measured to approach 1 (i.e., $0.93\text{--}0.99$, Table 3). However, the sole SnO_y support exhibits abundant Brønsted acid sites, in agreement with the literature [41]. More importantly, a volcano-like tendency can be observed for the Lewis acidity of the $\text{Sn}_x\text{Mn}_1\text{O}_y$ supports with the addition of Sn. The amount of Lewis acidity exhibits a maximum value ($411\text{ }\mu\text{mol g}^{-1}$) on the $\text{Sn}_{0.8}\text{Mn}_1\text{O}_y$ support, in consistent with NH_3 -TPD results.

Both hydrogenation sites and Lewis acidic sites are believed to be critical for GVL formation from LA [4]. The support effect of a $\text{Ni}/\text{Al}_2\text{O}_3$ and a Ni/ZrO_2 catalyst for hydrogenation of LA in vapor phase was investigated [42]. It was shown that Lewis acidic sites, as well as Brønsted acidic sites, on the support was responsible for dehydration of HPA to GVL. Moreover, it was evident for a $\text{Ru}/(\text{AlO})(\text{ZrO})_n$ catalyst that the high yield to GVL from LA was mainly attributed to the presence of Lewis acidic sites [27]. The NH_3 -TPD and adsorbed pyridine-IR results in this work reveal that the Lewis acidity is dominant for the total acidity of all the supports. Thereby, those strong Lewis acidic sites can be probably responsible for dehydration of HPA to GVL.

Following that, the metal-support interaction can be further elucidated. As shown by H_2 -TPR profiles (Fig. 8A), the redox property of the catalyst can be regularly modified upon the synergy in the $\text{Sn}_x\text{Mn}_1\text{O}_y$ support. The peak at a low temperature region ($100\text{--}200\text{ }^\circ\text{C}$) can be ascribed to the reduction of PtO to metallic Pt [43]. This peak of the $\text{Pt}/\text{Sn}_x\text{Mn}_1\text{O}_y$ catalyst is observed to clearly shift to a lower temperature in comparison with Pt/MnO_y (ca. $201\text{ }^\circ\text{C}$) and Pt/SnO_y (ca. $194\text{ }^\circ\text{C}$). Moreover, with increasing Sn the reduction temperature of PtO first declines and then rises and exhibits a lowest value for $\text{Pt}/\text{Sn}_{0.8}\text{Mn}_1\text{O}_y$. This phenomenon indicates that a strong metal-support interaction exists between Pt nanoparticles and the binary $\text{Sn}_x\text{Mn}_1\text{O}_y$ oxides, which can significantly improve the reduction of supported Pt on the unary oxides, and

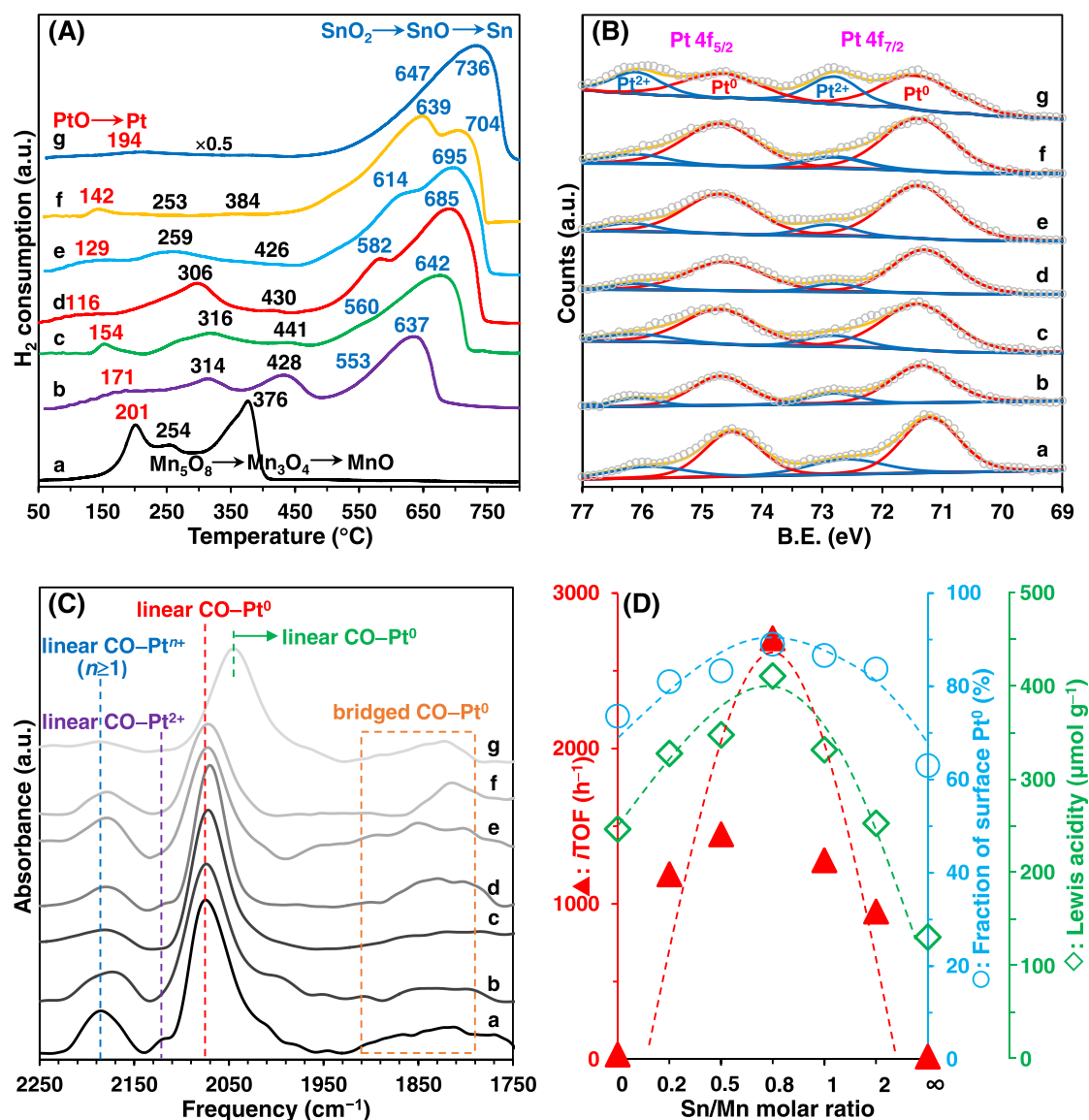


Fig. 8. (A) H₂-TPR profiles, (B) deconvoluted XPS spectra of Pt 4f core level, and (C) *in situ* DRIFT-IR spectra of CO adsorption after being purged with a He low for 30 min for the (a) Pt/MnO_y, (b) Pt/Sn_{0.2}Mn₁O_y, (c) Pt/Sn_{0.5}Mn₁O_y, (d) Pt/Sn_{0.8}Mn₁O_y, (e) Pt/Sn₁Mn₁O_y, (f) Pt/Sn₂Mn₁O_y, and (g) Pt/SnO_y catalysts. (D) Dependence of iTOF, the fraction of surface Pt⁰ species, and the Lewis acidity of support measured by pyridine adsorption IR on the Sn/Mn molar ratio in the Pt/Sn_xMn₁O_y catalyst.

particularly an enhanced reducibility is obtained on the Pt/Sn_{0.8}Mn₁O_y catalyst due to the optimal synergy between MnO_y and SnO_y. The peaks from moderate (250–500 °C) to high (500–800 °C) temperature regions can be related to the reduction of MnO_y and SnO_y, respectively. Specifically, Pt/MnO_y shows two peaks (ca. 254 and 376 °C) that can be assigned to the successive reduction of Mn₅O₈ → Mn₃O₄ → MnO [32], while Pt/SnO_y also displays two peaks (ca. 647 and 736 °C) that can be attributed to the successive reduction of SnO₂ → SnO → Sn [44]. Interestingly, increasing Sn in the Sn_xMn₁O_y support can generally facilitate the reduction of MnO_y but restrain that of SnO_y. However, compared to the unary oxides, it can be clearly seen for Sn_xMn₁O_y that the reduction of MnO_y is globally inhibited whereas that of SnO_y is promoted. This phenomenon demonstrates that the variable interactions between MnO_y and SnO_y can modify the redox property of the Sn_xMn₁O_y support.

XPS allows collecting more information on the surface of a catalyst. As reported in Fig. 8B, the Pt 4f core level exhibits two spin-orbit doublets due to Pt 4f_{7/2}–Pt 4f_{5/2}. For all the catalysts the binding energies (BEs) at ca. 71.4 and 72.8 eV in the Pt 4f_{7/2} region can be attributed to the typical Pt⁰ and Pt²⁺ species (Table S5) [45], respectively. Moreover, the

quantitative analysis shows a trend from rise to decline for the surface fraction of Pt⁰ (63–88.4%) and the highest value is measured on the Pt/Sn_{0.8}Mn₁O_y catalyst (Table 1). The Mn 2p_{3/2} core level can be resolved into three peaks with BEs at ca. 640.7 eV, 642.1 eV, 644.3 eV for the Pt/MnO_y catalyst, which can be ascribed to Mn²⁺, Mn³⁺ and Mn⁴⁺ ions (Fig. S1) [31], respectively. While for the Pt/SnO_y catalyst the Sn 3d_{5/2} core level with a BE at ca. 486.9 eV is characteristic of Sn⁴⁺ ions in SnO₂ (Fig. S1) [46]. Further inspection on the Pt/Sn_xMn₁O_y catalysts shows that the BEs of Mn ions slightly grows, in return those of Sn⁴⁺ ions reduce (Table S5). This indicates an electron transfer from Mn to Sn due to the metal interaction in the binary oxides. The O 1s core level can be resolved into two peaks (Fig. S1) that can correspond to the lattice oxygen species in an oxide (i.e., O²⁻, named as O_{latt}) and the adsorbed oxygen species on an oxide (i.e., O⁻ and O₂⁻, named as O_{ads}). [47]. The unsaturated O_{ads} species can usually lead to formation of oxygen vacancies on the surface of a catalyst [48], which has been reported to facilitate catalytic hydrogenation of LA by enhancing the adsorption and activation of the COOH or C=O groups in LA [49]. In this work, the fraction of O_{ads} species is found to follow the similar tendency to that of Pt⁰, presenting an optimal of 74%

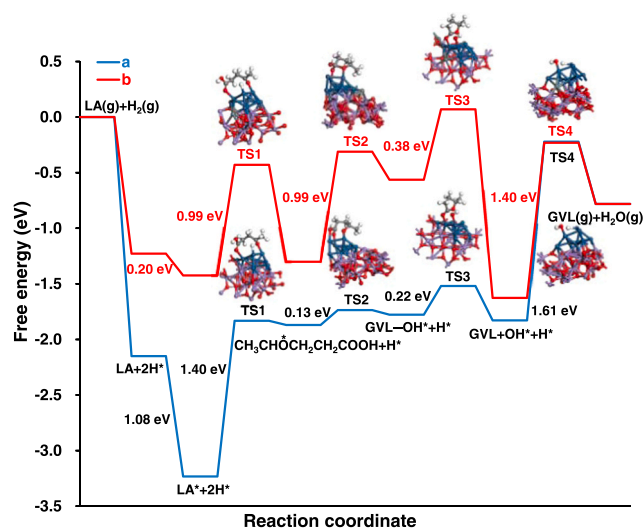


Fig. 9. Potential energy profiles for hydrogenation of LA to GVL over the (a) $\text{Pt}_9/\text{Mn}_3\text{O}_4$ and (b) $\text{Pt}_9/\text{Sn}_{0.8}\text{Mn}_{1.0}\text{O}_y$ model catalysts.

on the $\text{Pt}/\text{Sn}_{0.8}\text{Mn}_{1.0}\text{O}_y$ catalyst (Table S5).

To deeply clarify the metal-support interaction, an *in situ* DRIFT experiment is carried out using CO molecule as a probe. This technique is sensitive and informative to detecting only the exposed surface metal sites whereas the subsurface and bulk sites cannot be analyzed. As displayed in Fig. 8C, the relatively weak bands at 2122 and 2186 cm^{-1} can be assigned to the linear adsorption of CO on Pt^{2+} and Pt^{n+} ($n \geq 1$) species [50], respectively. In the lower frequency region, an intense band at ca. 2075 cm^{-1} can be attributed to the linear adsorption of CO on Pt^0 sites [51]. Moreover, this major band red-shifts (2–5 cm^{-1}) on the $\text{Pt}/\text{Sn}_x\text{Mn}_y\text{O}_z$ catalysts compared to Pt/MnO_y , and the maximum is observed on $\text{Pt}/\text{Sn}_{0.8}\text{Mn}_{1.0}\text{O}_y$. This implies a strong metal-support interaction due to an electron transfer from the $\text{Sn}_x\text{Mn}_y\text{O}_z$ supports to Pt [52], in agreement with H_2 -TPR results. For Pt/SnO_y , the major absorption band of linear CO– Pt^0 is located at ca. 2045 cm^{-1} , which is consistent with the literature [51]. In addition, several small bands at 1790–1910 cm^{-1} can be originated from the bridged adsorption of CO on Pt^0 sites [51,53]. Clearly, as the simplified model for C=O group, CO molecule can be well adsorbed on the Pt^0 active sites and this process is enhanced on the optimal $\text{Pt}/\text{Sn}_{0.8}\text{Mn}_{1.0}\text{O}_y$ catalyst.

3.5. Discussion on the structure-activity correlation and reaction mechanism

Based on the above results, the structure-activity correlation can be discussed. As shown in Fig. 8D, a typical volcano-like relationship can be established between the *i*TOF values and the Sn/Mn molar ratios. This relation reflects a strong dependence of the intrinsic activity of the surface Pt atoms on the variable Sn-Mn interactions in the support. Moreover, the fraction of surface Pt^0 species of a catalyst (*i.e.*, responsible for hydrogenation) and the Lewis acidity of a support (*i.e.*,

responsible for dehydration) displays a highly similar trend to that of *i*TOF. This result reveals that the number of Pt^0 species and Lewis acidic sites on the surface of a catalyst are decisive factors for the intrinsic activity. The highest activity of Pt sites can be only achieved by the enhanced Sn-Mn synergistic effect of the $\text{Sn}_x\text{Mn}_y\text{O}_z$ support with a suitable composition.

To further elaborate the crucial synergistic effect in the $\text{Sn}_{0.8}\text{Mn}_{1.0}\text{O}_y$ oxide on promoting the catalytic performance of the supported Pt nanoparticles, DFT calculations are performed. $\text{Pt}_9/\text{Mn}_3\text{O}_4$ and $\text{Pt}_9/\text{Sn}_{0.8}\text{Mn}_{1.0}\text{O}_y$ selected as the model catalysts are used to illustrate the reaction mechanism for hydrogenation of LA to GVL at molecular level. Previously, researchers from different groups proposed a reaction pathway with a lower activation energy barrier for this reaction [54,55], in which LA first hydrogenated to alkoxy intermediate (*i.e.*, $\text{CH}_3\text{CHOCH}_2\text{CH}_2\text{COOH}$), then it subsequently generated GVL–OH by the ring closure and finally formed GVL by dehydroxylation. Therefore, it can be reasonable for us to discuss the reaction mechanism by comparing the differences in adsorption energy, activation energy and reaction energy over the $\text{Pt}_9/\text{Mn}_3\text{O}_4$ and $\text{Pt}_9/\text{Sn}_{0.8}\text{Mn}_{1.0}\text{O}_y$ catalysts. DFT calculations show that the adsorption energy (–0.20 eV) for LA on $\text{Pt}_9/\text{Sn}_{0.8}\text{Mn}_{1.0}\text{O}_y$ is much weaker than that on $\text{Pt}_9/\text{Mn}_3\text{O}_4$ (–1.08 eV), which indicates that the hydrogenation of LA could be promoted over the $\text{Pt}_9/\text{Sn}_{0.8}\text{Mn}_{1.0}\text{O}_y$ catalyst in comparison with the Sn-absent $\text{Pt}_9/\text{Mn}_3\text{O}_4$ catalyst. The Sabatier principle states that too weak or too strong of an interaction between a catalyst surface and adsorbed species will result in poor catalytic activity. It was reported in literature that a moderate adsorption strength of LA promoted the hydrogenation of the C=O bond and the subsequent dehydration to produce GVL over the Co– MoO_x catalyst [56].

Fig. 9 displays the free energy diagram and TS configurations for hydrogenation of LA to GVL. Firstly the dissociation of H_2 to H^* can easily occur on Pt sites and shows nearly no additional barrier. In subsequence the hydrogenation of C=O group in LA by C–H bond formation to the $\text{CH}_3\text{CHOCH}_2\text{CH}_2\text{COOH}^*$ intermediate exhibits a high activation energy of 1.40 eV over $\text{Pt}_9/\text{Mn}_3\text{O}_4$. On the contrary, the activation energy of this step greatly declines to 0.99 eV with incorporation of Sn to the $\text{Pt}_9/\text{Mn}_3\text{O}_4$ catalyst, which illustrates that Sn is indispensable to promote this reaction. Notably, this initial step is considered to be critical for the overall reaction. Afterwards, $\text{CH}_3\text{CHOCH}_2\text{CH}_2\text{COOH}^*$ proceeds to generate GVL–OH* by cyclization. This step requires a moderate activation energy of 0.99 eV for $\text{Pt}_9/\text{Sn}_{0.8}\text{Mn}_{1.0}\text{O}_y$ but a lower one (0.13 eV) for $\text{Pt}_9/\text{Mn}_3\text{O}_4$. Following that, GVL is formed by the dehydroxylation of GVL–OH*, of which the activation barrier is calculated to be 0.38 and 0.22 eV for $\text{Pt}_9/\text{Sn}_{0.8}\text{Mn}_{1.0}\text{O}_y$ and $\text{Pt}_9/\text{Mn}_3\text{O}_4$, respectively. Finally, H_2O is produced by combining OH^* derived from the previous step with the nearby H^* . As shown by the kinetic experiments (Fig. 3), formation of H_2O can be rationally considered to be the rate determining step for hydrogenation of LA to GVL. Notably, $\text{Pt}_9/\text{Sn}_{0.8}\text{Mn}_{1.0}\text{O}_y$ shows an obviously lower energy barrier than that required by $\text{Pt}_9/\text{Mn}_3\text{O}_4$ (*i.e.*, 1.40 versus 1.61 eV). Therefore, DFT calculations demonstrate that the Sn-Mn synergy in the $\text{Sn}_{0.8}\text{Mn}_{1.0}\text{O}_y$ oxide can significantly facilitate the hydrogenation of LA to GVL on the supported Pt active sites, in good agreement with the experimental results.

Table 4
Comparison study on the supported Pt catalysts for hydrogenation of LA to GVL.

Catalyst	Conv. (%)	Select. (%)	Time (h)	<i>T</i> (°C)	<i>P</i> , H_2 (MPa)	Solvent	TOF (h^{-1})	Reuse times	Ref.
$\text{Pt}_1\text{Pd}_3/\text{SBA-15}$	94	>99	4	220	10	H_2O	3600	4	[23]
$\text{Pt}/\text{Sn}_{0.8}\text{Mn}_{1.0}\text{O}_y$	99	100	6	120	2	H_2O	2709	10 ^a	this work
$\text{PtNb}/\text{BP2000}$	not reported			180	4	H_2O	2376	2	[24]
$\text{Pt}/\text{Al}_2\text{O}_3$	94	100	5	70	0.13	H_2O	–	–	[22]
t-Au@Pt/G-CB	48	>99	0.5	120	2	H_2O	62	–	[57]
$\text{Pt}_{40}/\text{meso-SiO}_2$	88	98	5	150	1	H_2O	27.1	3	[20]
$\text{Pt}/\text{zeolite-Y}$	100	92	24	220	2.5	H_2O	13.5	–	[21]

^a The recycling experiments were conducted by using dioxane as solvent.

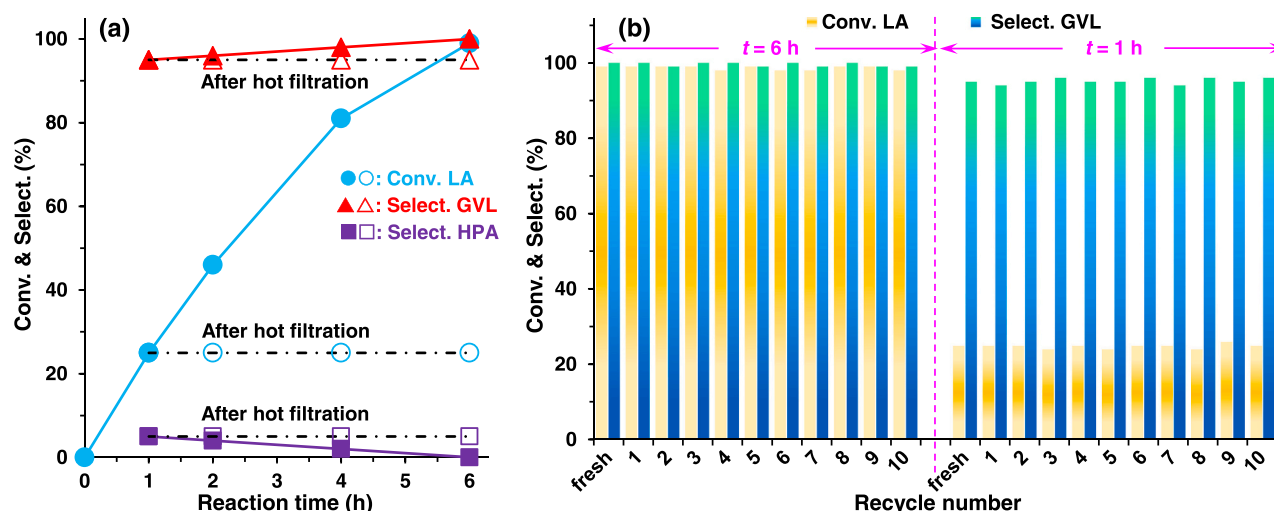


Fig. 10. (a) Leaching test for Pt after a hot filtration, and (b) recycling test for the Pt/Sn_{0.8}Mn₁O_y catalyst during hydrogenation of LA. Reaction conditions: catalyst, 50 mg; LA, 5 mmol; dioxane, 10 mL; H₂, 2.0 MPa; temperature, 120 °C.

3.6. Comparison study with the benchmark catalysts

The comparison study is done between the Pt/Sn_{0.8}Mn₁O_y catalyst and the supported Pt catalysts ever reported in the literature. Notably, for noble-metal catalysts a challenge of this reaction is to use water as reaction solvent. Water as a byproduct tends to block the forward reaction. Water may also aggravate metal leaching. Therefore, the reaction is conducted in water over the Pt/Sn_{0.8}Mn₁O_y catalyst. As summarized in Table 4, all the catalysts present a satisfying to excellent selectivity to GVL (92–100%) but very different conversions of LA (48–99%). It can be clearly seen that Pt/Sn_{0.8}Mn₁O_y in this work exhibits the best performance which is obtained at milder reaction conditions, that is, low temperature and pressure. Moreover, a very high TOF of 2709 h⁻¹ is achieved on the Pt/Sn_{0.8}Mn₁O_y catalyst, which is ca. 10–200 folds to the monometallic Pt catalysts. This activity can be even comparable to the bimetallic PtPd (3600 h⁻¹) and PtNb (2376 h⁻¹) catalysts that have to rely on the unique alloy effect and the harsh reaction conditions. Therefore, the developed Pt/Sn_{0.8}Mn₁O_y catalyst shows the most outstanding result reported in the literature to date.

3.7. Stability and reusability

Finally, the stability and reusability of the Pt/Sn_{0.8}Mn₁O_y catalyst is investigated, which is regarded to be important to a heterogeneous catalyst for the sake of cost control and practical application. Firstly the possible leaching of Pt from the catalyst is verified by a hot-filtration process. Conversion of LA and distribution of products are found unchanged when the catalyst is removed at 1 h and the liquid is stirred at 120 °C in the presence of H₂ for another 5 h (Fig. 10a). This result indicates no loss of active Pt component from the catalyst into the reaction mixture. It is thereafter confirmed by ICP-MS analysis on Pt as well as Sn and Mn from the postreaction solution. And then the used and post-treated Pt/Sn_{0.8}Mn₁O_y catalyst (see experimental details) is tested in a consecutive recycling experiment and shows a remarkable stability after ten cycles under the regular reaction conditions (Fig. 10b). Furthermore, the stability is verified within the kinetic-controlled region, because any deactivation of a catalyst can be easily reflected during the initial stage. As shown in Fig. 10b, Pt/Sn_{0.8}Mn₁O_y also displays an excellent performance. In addition, TEM, XPS and NH₃-TPD are used to analyze the property of the used catalyst (Fig. S2). It is evident that the dispersion and valence state of Pt nanoparticles, as well as the acidic property, of the used catalyst can be maintained in comparison with those of its fresh state. This may be responsible for the superior stability and reusability of

the Pt/Sn_{0.8}Mn₁O_y catalyst.

4. Conclusions

In summary, the synergistic effect between Sn and Mn in a Sn_xMn₁O_y oxide is shown to boost the hydrogenation catalysis of supported Pt nanoparticles for selective conversion of LA to GVL. Incorporating a variable loading of Sn to the MnO_y oxide allows regularly modifying the Lewis acidic properties of the binary Sn_xMn₁O_y oxides. Meanwhile, the synergistic effect between MnO_y and SnO_y is demonstrated to enhance the Pt-Sn_xMn₁O_y interaction that can stabilize a vast active Pt⁰ species. The *in situ* catalytic reaction reveals that LA undergoes a successive hydrogenation-dehydration pathway via HPA as the intermediate. Thereby, the unique catalytic property can promote the tandem catalysis from hydrogenation of LA on Pt⁰ sites and dehydration of HPA to GVL on Lewis acidic sites over the Pt/Sn_xMn₁O_y catalyst. In addition, the theoretical study by DFT calculations further elucidates that the incorporation of Sn to MnO_y is indispensable to facilitate this reaction. Hydrogenation of LA to an alkoxy intermediate and formation of H₂O by ring-closure are considered to be the crucial steps for the overall reaction, and the addition of Sn can provide obviously a lower energy barrier for both steps.

CRediT authorship contribution statement

Yaowei Lu: Investigation, Methodology, Formal analysis, Writing – original draft preparation. **Yongxing Wang:** Validation, Formal analysis. **Qinghu Tang:** Methodology, Funding acquisition. **Qiue Cao:** Resources, Supervision. **Wenhao Fang:** Conceptualization, Resources, Supervision, Writing – review & editing, Project administration, Funding acquisition.

Declaration of Competing Interest

The authors declare that they have no known competing financial interests or personal relationships that could have appeared to influence the work reported in this paper.

Acknowledgements

This work was supported by the National Natural Science Foundation of China, China (No. 21763031 and 22062025); the Yunnan Fundamental Research Projects, China (No. 202001AW070012,

202101AT070171); the National Special Funds of China, China (No. C176220100063); the Program for Excellent Young Talents of Yunnan University, China; and the Open Research Fund of School of Chemistry and Chemical Engineering of Henan Normal University, China. The authors thank Advanced Analysis and Measurement Center of Yunnan University for the sample testing service.

Appendix A. Supporting information

Supplementary data associated with this article can be found in the online version at doi:10.1016/j.apcatb.2021.120746.

References

- [1] A. Corma, S. Iborra, A. Velty, Chemical routes for the transformation of biomass into chemicals, *Chem. Rev.* 107 (2007) 2411–2502.
- [2] X. Wu, N. Luo, S. Xie, H. Zhang, Q. Zhang, F. Wang, Y. Wang, Photocatalytic transformations of lignocellulosic biomass into chemicals, *Chem. Soc. Rev.* 49 (2020) 6198–6223.
- [3] S. Zhu, H. Liu, S. Wang, X. Gao, P. Wang, J. Wang, W. Fan, One-step efficient non-hydrogen conversion of cellulose into γ -valerolactone over AgPW/CoNi@NG composite, *Appl. Catal. B: Environ.* 284 (2021), 119698.
- [4] F. Liguori, C. Moreno-Marrodan, P. Barbaro, Environmentally friendly synthesis of γ -valerolactone by direct catalytic conversion of renewable sources, *ACS Catal.* 5 (2015) 1882–1894.
- [5] H. Wang, Y. Wu, Y. Li, J. Peng, X.-K. Gu, M. Ding, SARS-CoV-2 has the advantage of competing the iMet-tRNAs with human hosts to allow efficient translation, *Mol. Genet. Genom.* 296 (2021) 113–118.
- [6] I.T. Horváth, Solvents from nature, *Green. Chem.* 10 (2008) 1024–1028.
- [7] S.G. Wettstein, J.Q. Bond, D.M. Alonso, H.N. Pham, A.K. Datye, J.A. Dumesic, RuSn bimetallic catalysts for selective hydrogenation of levulinic acid to γ -valerolactone, *Appl. Catal. B* 117–118 (2012) 321–329.
- [8] J. Tan, J. Cui, X. Cui, T. Deng, X. Li, Y. Zhu, Y. Li, Graphene-modified Ru nanocatalyst for low-temperature hydrogenation of carbonyl groups, *ACS Catal.* 5 (2015) 7379–7384.
- [9] S. Song, S. Yao, J. Cao, L. Di, G. Wu, N. Guan, L. Li, Heterostructured Ni/NiO composite as a robust catalyst for the hydrogenation of levulinic acid to γ -valerolactone, *Appl. Catal. B* 217 (2017) 115–124.
- [10] W. Cao, L. Lin, H. Qi, Q. He, Z. Wu, A. Wang, W. Luo, T. Zhang, In-situ synthesis of single-atom Ir by utilizing metal-organic frameworks: an acid-resistant catalyst for hydrogenation of levulinic acid to γ -valerolactone, *J. Catal.* 373 (2019) 161–172.
- [11] X. Huang, K. Liu, W.L. Vrijburg, X. Ouyang, A. Iulian Dugulan, Y. Liu, M.W.G. M. Tiny Verhoeven, N.A. Kosinov, E.A. Pidko, E.J.M. Hensen, Hydrogenation of levulinic acid to γ -valerolactone over Fe-Re/TiO₂ catalysts, *Appl. Catal. B: Environ.* 278 (2020), 119314.
- [12] J.B.G. Filho, R.D.F. Rios, C.G.O. Bruziquesi, D.C. Ferreira, H.F.V. Victória, K. Krambrock, M.C. Pereira, L.C.A. Oliveira, A promising approach to transform levulinic acid into γ -valerolactone using niobic acid photocatalyst and the accumulated electron transfer technique, *Appl. Catal. B: Environ.* 285 (2021), 119814.
- [13] J.J. Bozell, L. Moens, D.C. Elliott, Y. Wang, G.G. Neuenschwander, S.W. Fitzpatrick, R.J. Bliski, J.L. Jarnefeld, Production of levulinic acid and use as a platform chemical for derived products, *Resour., Conserv. Recycl.* 28 (2000) 227–239.
- [14] O.A. Abdelrahman, A. Heyden, J.Q. Bond, Analysis of kinetics and reaction pathways in the aqueous-phase hydrogenation of levulinic acid to form γ -valerolactone over Ru/C, *ACS Catal.* 4 (2014) 1171–1181.
- [15] I. Ro, I.B. Aragao, Z.J. Brentzel, Y. Liu, K.R. Rivera-Dones, M.R. Ball, D. Zanchet, G. W. Huber, J.A. Dumesic, Intrinsic activity of interfacial sites for Pt-Fe and Pt-Mo catalysts in the hydrogenation of carbonyl groups, *Appl. Catal. B* 231 (2018) 182–190.
- [16] E. Yik, D. Hibbitts, H. Wang, E. Iglesia, Hydrogenation and C-S bond activation pathways in thiophene and tetrahydrothiophene reactions on sulfur-passivated surfaces of Ru, Pt, and Re nanoparticulates, *Appl. Catal. B: Environ.* 291 (2021), 119797.
- [17] K. Su, Y. Wang, C. Zhang, Z. Gao, J. Han, F. Wang, Tuning the Pt species on Nb₂O₅ by support-induced modification in the photocatalytic transfer hydrogenation of phenylacetylene, *Appl. Catal. B: Environ.* 298 (2021), 120554.
- [18] H.J. Cho, D. Kim, J. Li, D. Su, B. Xu, Zeolite-encapsulated Pt nanoparticles for tandem catalysis, *J. Am. Chem. Soc.* 140 (2018) 13514–13520.
- [19] H.J. Cho, D. Kim, S. Li, D. Su, D. Ma, B. Xu, Molecular-level proximity of metal and acid sites in zeolite-encapsulated Pt nanoparticles for selective multistep tandem catalysis, *ACS Catal.* 10 (2020) 3340–3348.
- [20] M. Nemanashi, J.-H. Noh, R. Meijboom, Hydrogenation of biomass-derived levulinic acid to γ -valerolactone catalyzed by mesoporous supported dendrimer-derived Ru and Pt catalysts: an alternative method for the production of renewable biofuels, *Appl. Catal. A* 550 (2018) 77–89.
- [21] H.-T. Vu, F.M. Harth, N. Wilde, Silylated zeolites with enhanced hydrothermal stability for the aqueous-phase hydrogenation of levulinic acid to γ -valerolactone, *Front. Chem.* 6 (2018) 143.
- [22] R.Y. Parapat, F.A. Yudatama, M.R. Musadi, M. Schwarze, R. Schomäcker, Antioxidant as structure directing agent in nanocatalyst preparation. case study: catalytic activity of supported Pt nanocatalyst in levulinic acid hydrogenation, *Ind. Eng. Chem. Res.* 58 (2019) 2460–2470.
- [23] Y. Qiao, N. Said, M. Rauser, K. Yan, F. Qin, N. Theyssen, W. Leitner, Preparation of SBA-15 supported Pt/Pd bimetallic catalysts using supercritical fluid reactive deposition: how do solvent effects during material synthesis affect catalytic properties? *Green. Chem.* 19 (2017) 977–986.
- [24] S.-L. Xu, S.-C. Shen, W. Xiong, S. Zhao, L.-J. Zuo, L. Wang, W.-J. Zeng, S.-Q. Chu, P. Chen, Y. Lin, K. Qian, W. Huang, H.-W. Liang, High-temperature synthesis of small-sized Pt/Nb alloy catalysts on carbon supports for hydrothermal reactions, *Inorg. Chem.* 59 (2020) 15953–15961.
- [25] A.S. Touchy, S.M.A. Hakim Siddiki, K. Kon, K.-I. Shimizu, Heterogeneous Pt catalysts for reductive amination of levulinic acid to pyrrolidones, *ACS Catal.* 4 (2014) 3045–3050.
- [26] Z.-S. Zhang, Q. Fu, K. Xu, W.-W. Wang, X.-P. Fu, X.-S. Zheng, K. Wu, C. Ma, R. Si, C.-J. Jia, L.-D. Sun, C.-H. Yan, Intrinsically active surface in a Pt/ γ -Mo₂N catalyst for the water–gas shift reaction: molybdenum nitride or molybdenum oxide? *J. Am. Chem. Soc.* 142 (2020) 13362–13371.
- [27] Y. Lu, Y. Wang, Y. Wang, Q. Cao, X. Xie, W. Fang, Hydrogenation of levulinic acid to γ -valerolactone over bifunctional Ru/(AlO)(ZrO)_x catalyst: Effective control of Lewis acidity and surface synergy, *Mol. Catal.* 493 (2020), 111097.
- [28] G. Novodárszki, H.E. Solt, J. Valyon, F. Lónyi, J. Hancsók, D. Deka, R. Tuba, M. R. Mihályi, Selective hydroconversion of levulinic acid to γ -valerolactone or 2-methyltetrahydrofuran over silica-supported cobalt catalysts, *Catal. Sci. Technol.* 9 (2019) 2291–2304.
- [29] G. Zhang, W. Li, G. Fan, L. Yang, F. Li, Controlling product selectivity by surface defects over MoO₃-decorated Ni-based nanocatalysts for γ -valerolactone hydrogenolysis, *J. Catal.* 379 (2019) 100–111.
- [30] D. Reichert, A. Montoya, X. Liang, H. Bockhorn, B.S. Haynes, Conformational and thermodynamic properties of gaseous levulinic acid, *J. Phys. Chem. A* 114 (2010) 12323–12329.
- [31] T. Gao, J. Chen, W. Fang, Q. Cao, W. Su, F. Dumeignil, Ru/Mn_xCe_{1-x}O_y catalysts with enhanced oxygen mobility and strong metal-support interaction: exceptional performances in 5-hydroxymethylfurfural base-free aerobic oxidation, *J. Catal.* 368 (2018) 53–68.
- [32] T. Gao, Y. Yin, G. Zhu, Q. Cao, W. Fang, Co₃O₄ NPs decorated Mn-Co-O solid solution as highly selective catalyst for aerobic base-free oxidation of 5-HMF to 2,5-FDCA in water, *Catal. Today* 355 (2020) 252–262.
- [33] H. Deng, J.M. Hosselopp, Combined X-ray diffraction and diffuse reflectance analysis of nanocrystalline mixed Sn(II) and Sn(IV) oxide powders, *J. Phys. Chem. B* 109 (2005) 66–73.
- [34] S. Wu, H. Zhang, Q. Cao, Q. Zhao, W. Fang, Efficient imine synthesis via oxidative coupling of alcohols with amines in an air atmosphere using a mesoporous manganese-zirconium solid solution catalyst, *Catal. Sci. Technol.* 11 (2021) 810–822.
- [35] W. Fang, Y. Romani, Y. Wei, M. Jiménez-Ruiz, H. Jobic, S. Paul, L. Jalowiecki-Duhamel, Steam reforming and oxidative steam reforming for hydrogen production from bioethanol over Mg₂AlNi₄H₂O₇ nano-oxyhydride catalysts, *Int. J. Hydrog. Energy* 43 (2018) 17643–17655.
- [36] Y. Lu, X. Xie, W. Fang, Insight into the property modification of Zr-incorporated alumina binary mixed oxides by XRD, TEM, XPS, TPD and IR, *ChemistrySelect* 5 (2020) 7928–7933.
- [37] T. Odom-Wubah, Q. Li, I. Adilov, J. Huang, Q. Li, Towards efficient Pd/Mn₃O₄ catalyst with enhanced acidic sites and low temperature reducibility for Benzene abatement, *Mol. Catal.* 477 (2019), 110558.
- [38] E. Fernández López, V. Sánchez Escribano, C. Resini, J.M. Gallardo-Amores, G. Busca, A study of coprecipitated Mn–Zr oxides and their behaviour as oxidation catalysts, *Appl. Catal. B* 29 (2001) 251–261.
- [39] M. Rumyantseva, V. Kovalenko, A. Gaskov, E. Makshina, V. Yuschenko, I. Ivanova, A. Ponzoni, G. Faglia, E. Comini, Nanocomposites SnO₂/Fe₂O₃: sensor and catalytic properties, *Sens. Actuators B: Chem.* 118 (2006) 208–214.
- [40] M.W. Abee, D.F. Cox, NH₃ chemisorption on stoichiometric and oxygen-deficient SnO₂(110) surfaces, *Surf. Sci.* 520 (2002) 65–77.
- [41] B. Mallesham, P. Sudarsanam, G. Raju, B.M. Reddy, Design of highly efficient Mo and W-promoted SnO₂ solid acids for heterogeneous catalysis: acetalization of bioglycerol, *Green. Chem.* 15 (2013) 478–489.
- [42] V. Mohan, V. Venkateshwarlu, C.V. Pramod, B.D. Raju, K.S.R. Rao, Vapour phase hydrocyclisation of levulinic acid to γ -valerolactone over supported Ni catalysts, *Catal. Sci. Technol.* 4 (2014) 1253–1259.
- [43] R. Kouraichi, J.J. Delgado, J.D. López-Castro, M. Stitou, J.M. Rodríguez-Izquierdo, M.A. Cauqui, Deactivation of Pt/MnO_x-CeO₂ catalysts for the catalytic wet oxidation of phenol: formation of carbonaceous deposits and leaching of manganese, *Catal. Today* 154 (2010) 195–201.
- [44] Y. Liu, Y. Guo, Y. Liu, X. Xu, H. Peng, X. Fang, X. Wang, SnO₂ nano-rods promoted by In, Cr and Al cations for toluene total oxidation: The impact of oxygen property and surface acidity on the catalytic activity, *Appl. Surf. Sci.* 420 (2017) 186–195.
- [45] N. An, Q. Yu, G. Liu, S. Li, M. Jia, W. Zhang, Complete oxidation of formaldehyde at ambient temperature over supported Pt/Fe₂O₃ catalysts prepared by colloid-deposition method, *J. Hazard. Mater.* 186 (2011) 1392–1397.
- [46] W. Sun, S. Wu, Y. Lu, Y. Wang, Q. Cao, W. Fang, Effective control of particle size and electron density of Pd/C and Sn-Pd/C nanocatalysts for vanillin production via base-free oxidation, *ACS Catal.* 10 (2020) 7699–7709.
- [47] Y. Wang, Y. Lu, Q. Cao, W. Fang, A magnetic CoRu–CoO_x nanocomposite efficiently hydrogenates furfural to furfuryl alcohol at ambient H₂ pressure in water, *Chem. Commun.* 56 (2020) 3765–3768.
- [48] T. Gao, H. Zhang, C. Hu, F. Jing, W. Fang, Base-free aerobic oxidation of 5-hydroxymethylfurfural on a Ru(0) center in cooperation with a Co(II)/Co(III) redox

- pair over the one-pot synthesized Ru-Co composites, *Ind. Eng. Chem. Res.* 59 (2020) 17200–17209.
- [49] J. Li, M. Li, C. Zhang, C.-L. Liu, R.-Z. Yang, W.-S. Dong, Construction of mesoporous Cu/ZrO₂-Al₂O₃ as a ternary catalyst for efficient synthesis of γ -valerolactone from levulinic acid at low temperature, *J. Catal.* 381 (2020) 163–174.
- [50] H. Zhang, T. Gao, Q. Cao, W. Fang, Tailoring the reactive oxygen species in mesoporous NiO for selectivity-controlled aerobic oxidation of 5-hydroxymethylfurfural on a loaded Pt catalyst, *ACS Sustain. Chem. Eng.* 9 (2021) 6056–6067.
- [51] M.J. Kale, P. Christopher, Utilizing quantitative in situ FTIR spectroscopy to identify well-coordinated Pt atoms as the active site for CO oxidation on Al₂O₃-supported Pt catalysts, *ACS Catal.* 6 (2016) 5599–5609.
- [52] Y. Wang, Y. Wang, Y. Lu, Q. Cao, W. Fang, Efficient hydrogenation of 5-hydroxymethylfurfural using a synergistically bimetallic Ru-Ir/C catalyst, *Chem. Commun.* 57 (2021) 1742–1745.
- [53] S.K. Cheah, V.P. Bernardet, A.A. Franco, O. Lemaire, P. Gelin, Study of CO and hydrogen interactions on carbon-supported Pt nanoparticles by quadrupole mass spectrometry and operando diffuse reflectance FTIR spectroscopy, *J. Phys. Chem. C* 117 (2013) 22756–22767.
- [54] O. Mamun, E. Walker, M. Faheem, J.Q. Bond, A. Heyden, Theoretical investigation of the hydrodeoxygenation of levulinic acid to γ -valerolactone over Ru(0001), *ACS Catal.* 7 (2017) 215–228.
- [55] X. Gao, S. Zhu, M. Dong, J. Wang, W. Fan, Ru nanoparticles deposited on ultrathin TiO₂ nanosheets as highly active catalyst for levulinic acid hydrogenation to γ -valerolactone, *Appl. Catal. B: Environ.* 259 (2019), 118076.
- [56] L. Wang, Y. Yang, P. Yin, Z. Ren, W. Liu, Z. Tian, Y. Zhang, E. Xu, J. Yin, M. Wei, MoO_x-decorated Co-based catalysts toward the hydrodeoxygenation reaction of biomass-derived platform molecules, *ACS Appl. Mater. Interf.* 13 (2021) 31799–31807.
- [57] C. Engelbrekt, N. Šešelj, R. Poreddy, A. Riisager, J. Ulstrup, J. Zhang, Atomically thin Pt shells on Au nanoparticle cores: facile synthesis and efficient synergistic catalysis, *J. Mater. Chem. A* 4 (2016) 3278–3286.